
Woodbury Transformations for Deep Generative Flows

You Lu

Department of Computer Science
Virginia Tech
Blacksburg, VA
you.lu@vt.edu

Bert Huang

Department of Computer Science
Tufts University
Medford, MA
bert@cs.tufts.edu

Abstract

Normalizing flows are deep generative models that allow efficient likelihood calculation and sampling. The core requirement for this advantage is that they are constructed using functions that can be efficiently inverted and for which the determinant of the function's Jacobian can be efficiently computed. Researchers have introduced various such flow operations, but few of these allow rich interactions among variables without incurring significant computational costs. In this paper, we introduce *Woodbury transformations*, which achieve efficient invertibility via the Woodbury matrix identity and efficient determinant calculation via Sylvester's determinant identity. In contrast with other operations used in state-of-the-art normalizing flows, Woodbury transformations enable (1) high-dimensional interactions, (2) efficient sampling, and (3) efficient likelihood evaluation. Other similar operations, such as 1×1 convolutions, emerging convolutions, or periodic convolutions allow at most two of these three advantages. In our experiments on multiple image datasets, we find that Woodbury transformations allow learning of higher-likelihood models than other flow architectures while still enjoying their efficiency advantages.

1 Introduction

Deep generative models are powerful tools for modeling complex distributions and have been applied to many tasks such as synthetic data generation [27, 39], domain adaption [40], and structured prediction [33]. Examples of these models include autoregressive models [13, 28], variational autoencoders [21, 31], generative adversarial networks [11], and normalizing flows [6, 7, 22, 30]. Normalizing flows are special because of two advantages: They allow efficient and exact computation of log-likelihood and sampling.

Flow-based models are composed of a series of invertible functions, which are specifically designed so that their inverse and determinant of the Jacobian are easy to compute. However, to preserve this computational efficiency, these functions usually cannot sufficiently encode dependencies among dimensions of a variable. For example, affine coupling layers [6] split a variable to two parts and require the second part to only depend on the first. But they ignore the dependencies among dimensions in the second part.

To address this problem, Dinh et al. [6, 7] introduced a fixed permutation operation that reverses the ordering of the channels of pixel variables. Kingma and Dhariwal [22] introduced a 1×1 convolution, which are a generalized permutation layer, that uses a weight matrix to model the interactions among dimensions along the channel axis. Their experiments demonstrate the importance of capturing dependencies among dimensions. Relatedly, Hoogeboom et al. [15] proposed emerging convolution

operations, and Hoogeboom et al. [15] and Finz et al. [9] proposed periodic convolution. These two convolution layers have $d \times d$ kernels that can model dependencies along the spatial axes in addition to the channel axis. However, the increase in representational power comes at a cost: These convolution operations do not scale well to high-dimensional variables. The emerging convolution is a combination of two autoregressive convolutions [10, 23], whose inverse is not parallelizable. To compute the inverse or determinant of the Jacobian, the periodic convolution requires transforming the input and the convolution kernel to Fourier space. This transformation is computationally costly.

In this paper, we develop *Woodbury transformations* for generative flows. Our method is also a generalized permutation layer and uses spatial and channel transformations to model dependencies among dimensions along spatial and channel axes. We use the Woodbury matrix identity [37] and Sylvester’s determinant identity [35] to compute the inverse and Jacobian determinant, respectively, so that both the training and sampling time complexities are linear to the input variable’s size. We also develop a memory-efficient variant of the Woodbury transformation, which has the same advantage as the full transformation but uses significantly reduced memory when the variable is high-dimensional. In our experiments, we found that Woodbury transformations enable model quality comparable to many state-of-the-art flow architectures while maintaining significant efficiency advantages.

2 Deep Generative Flows

In this section, we briefly introduce the deep generative flows. More background knowledge can be found in the appendix.

A normalizing flow [30] is composed of a series of invertible functions $\mathbf{f} = \mathbf{f}_1 \circ \mathbf{f}_2 \circ \dots \circ \mathbf{f}_K$, which transform \mathbf{x} to a latent code \mathbf{z} drawn from a simple distribution. Therefore, with the *change of variables* formula, we can rewrite the log-likelihood $\log p_\theta(\mathbf{x})$ to be

$$\log p_\theta(\mathbf{x}) = \log p_Z(\mathbf{z}) + \sum_{i=1}^K \log \left| \det \left(\frac{\partial \mathbf{f}_i}{\partial \mathbf{r}_{i-1}} \right) \right|, \quad (1)$$

where $\mathbf{r}_i = \mathbf{f}_i(\mathbf{r}_{i-1})$, $\mathbf{r}_0 = \mathbf{x}$, and $\mathbf{r}_K = \mathbf{z}$.

Flow-based generative models [6, 7, 22] are developed on the theory of normalizing flows. Each transformation function used in the models is a specifically designed neural network that has a tractable Jacobian determinant and inverse. We can sample from a trained flow \mathbf{f} by computing $\mathbf{z} \sim p_Z(\mathbf{z})$, $\mathbf{x} = \mathbf{f}^{-1}(\mathbf{z})$.

There have been many operations, i.e., layers, proposed in recent years for generative flows. In this section, we discuss some commonly used ones, and more related works will be discussed in Section 4.

Actnorm layers [22] perform per-channel affine transformations of the activations using scale and bias parameters to improve training stability and performance. The actnorm is formally expressed as $\mathbf{y}_{:,i,j} = \mathbf{s} \odot \mathbf{x}_{:,i,j} + \mathbf{b}$, where both the input \mathbf{x} and the output \mathbf{y} are $c \times h \times w$ tensors, c is the channel dimension, and $h \times w$ are spatial dimensions. The parameters \mathbf{s} and \mathbf{b} are $c \times 1$ vectors.

Affine coupling layers [6, 7] split the input \mathbf{x} into two parts, $\mathbf{x}_a, \mathbf{x}_b$. And then fix \mathbf{x}_a and force \mathbf{x}_b to only relate to \mathbf{x}_a , so that the Jacobian is a triangular matrix. Formally, we compute

$$\begin{aligned} \mathbf{x}_a, \mathbf{x}_b &= \text{split}(\mathbf{x}), & \mathbf{y}_a &= \mathbf{x}_a, \\ \mathbf{y}_b &= \mathbf{s}(\mathbf{x}_a) \odot \mathbf{x}_b + \mathbf{b}(\mathbf{x}_a), & \mathbf{y} &= \text{concat}(\mathbf{y}_a, \mathbf{y}_b), \end{aligned}$$

where \mathbf{s} and \mathbf{b} are two neural networks with \mathbf{x}_a as input. The split and the concat split and concatenate the variables along the channel axis. Usually, \mathbf{s} is restricted to be positive. An additive coupling layer is a special case when $\mathbf{s} = \mathbf{1}$.

Actnorm layers only rescale the dimensions of \mathbf{x} , and affine coupling layers only relate \mathbf{x}_b to \mathbf{x}_a but omit dependencies among different dimensions of \mathbf{x}_b . Thus, we need other layers to capture local dependencies among dimensions.

Invertible convolutional layers [9, 15, 22] are generalized permutation layers that can capture correlations among dimensions. The 1×1 convolution [22] is $\mathbf{y}_{:,i,j} = \mathbf{M}\mathbf{x}_{:,i,j}$, where \mathbf{M} is a $c \times c$ matrix. The Jacobian of a 1×1 convolution is a block diagonal matrix, so that its log-determinant is $hw \log |\det(\mathbf{M})|$. Note that the 1×1 convolution only operates along the channel axis and ignores the dependencies along the spatial axes.

Emerging convolutions [15] combine two autoregressive convolutions [10, 23]. Each autoregressive convolution masks out some weights to force an autoregressive structure, so that the Jacobian is a triangular matrix and computing its determinant is efficient. One problem of emerging convolution is the computation of inverse is non-parallelizable, so that is inefficient for high-dimensional variables.

Periodic convolutions [9, 15] transform the input and kernel to the Fourier domain using discrete Fourier transformations, so the convolution function is an element-wise matrix product with a block-diagonal Jacobian. The computational cost of periodic convolutions is $\mathcal{O}(chw \log(hw) + c^3hw)$. Thus, when the input is high-dimensional, both training and sampling are expensive.

Multi-scale architectures [7] compose flow layers to generate rich models, using *split layers* to factor out variables and *squeeze layers* to shuffle dimensions, resulting in an architecture with K flow steps and L levels. See Fig. 1.

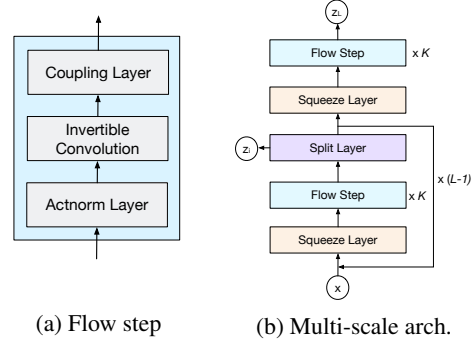


Figure 1: Overview of architecture of generative flows. We can design the flow step by selecting a suitable convolutional layer and a coupling layer based on the task. Glow [22] uses 1×1 convolutions and affine coupling.

3 Woodbury Transformations

In this section, we introduce Woodbury transformations as an efficient means to model high-dimensional correlations.

3.1 Channel and Spatial Transformations

Suppose we reshape the input \mathbf{x} to be a $c \times n$ matrix, where $n = hw$. Then the 1×1 convolution can be reinterpreted as a matrix transformation

$$\mathbf{y} = \mathbf{W}^{(c)}\mathbf{x}, \quad (2)$$

where \mathbf{y} is also a $c \times n$ matrix, and $\mathbf{W}^{(c)}$ is a $c \times c$ matrix. For consistency, we will call this a channel transformation. For each column $\mathbf{x}_{:,i}$, the correlations among channels are modeled by $\mathbf{W}^{(c)}$. However, the correlation between any two rows $\mathbf{x}_{:,i}$ and $\mathbf{x}_{:,j}$ is not captured. Inspired by Eq. 2, we use a spatial transformation to model interactions among dimensions along the spatial axis

$$\mathbf{y} = \mathbf{x}\mathbf{W}^{(s)}, \quad (3)$$

where $\mathbf{W}^{(s)}$ is an $n \times n$ matrix that models the correlations of each row $\mathbf{x}_{i,:}$. Combining Equation 2 and Equation 3, we have

$$\mathbf{x}_c = \mathbf{W}^{(c)}\mathbf{x}, \quad \mathbf{y} = \mathbf{x}_c\mathbf{W}^{(s)}. \quad (4)$$

For each dimension of output $\mathbf{y}_{i,j}$, we have $\mathbf{y}_{i,j} = \sum_{v=1}^c \left(\sum_{u=1}^n \mathbf{W}_{i,u}^{(c)} \cdot \mathbf{x}_{u,v} \right) \cdot \mathbf{W}_{v,j}^{(s)}$.

Therefore, the spatial and channel transformations together can model the correlation between any pair of dimensions. However, in this preliminary form, directly using Eq. 4 is inefficient for large c or n . First, we would have to store two large matrices \mathbf{W}^c and \mathbf{W}^s , so the space cost is $\mathcal{O}(c^2 + n^2)$. Second, the computational cost of Eq. 4 is $\mathcal{O}(c^2n + n^2c)$ —quadratic in the input size. Third, the computational cost of the Jacobian determinant is $\mathcal{O}(c^3 + n^3)$, which is far too expensive in practice.

3.2 Woodbury Transformations

We solve the three scalability problems by using a low-rank factorization. Specifically, we define

$$\mathbf{W}^{(c)} = \mathbf{I}^{(c)} + \mathbf{U}^{(c)}\mathbf{V}^{(c)}, \quad \mathbf{W}^{(s)} = \mathbf{I}^{(s)} + \mathbf{U}^{(s)}\mathbf{V}^{(s)},$$

where $\mathbf{I}^{(c)}$ and $\mathbf{I}^{(s)}$ are c - and n -dimensional identity matrices, respectively. The matrices \mathbf{U}^c , \mathbf{V}^c , \mathbf{U}^s , and \mathbf{V}^s are of size $c \times d_c$, $d_c \times c$, $n \times d_s$, and $d_s \times n$, respectively, where d_c and d_s are constant latent dimensions of these four matrices. Therefore, we can rewrite Equation 4 as

$$\mathbf{x}_c = (\mathbf{I}^{(c)} + \mathbf{U}^{(c)}\mathbf{V}^{(c)})\mathbf{x}, \quad \mathbf{y} = \mathbf{x}_c(\mathbf{I}^{(s)} + \mathbf{U}^{(s)}\mathbf{V}^{(s)}). \quad (5)$$

We call Eq. 5 the Woodbury transformation because the Woodbury matrix identity [37] and Sylvester’s determinant identity [35] allow efficient computation of its inverse and Jacobian determinant.

Woodbury matrix identity.¹ Let $\mathbf{I}^{(n)}$ and $\mathbf{I}^{(k)}$ be n - and k -dimensional identity matrices, respectively. Let \mathbf{U} and \mathbf{V} be $n \times k$ and $k \times n$ matrices, respectively. If $\mathbf{I}^{(k)} + \mathbf{V}\mathbf{U}$ is invertible, then $(\mathbf{I}^{(n)} + \mathbf{U}\mathbf{V})^{-1} = \mathbf{I}^{(n)} - \mathbf{U}(\mathbf{I}^{(k)} + \mathbf{V}\mathbf{U})^{-1}\mathbf{V}$.

Sylvester’s determinant identity. Let $\mathbf{I}^{(n)}$ and $\mathbf{I}^{(k)}$ be n - and k -dimensional identity matrices, respectively. Let \mathbf{U} and \mathbf{V} be $n \times k$ and $k \times n$ matrices, respectively. Then, $\det(\mathbf{I}^{(n)} + \mathbf{U}\mathbf{V}) = \det(\mathbf{I}^{(k)} + \mathbf{V}\mathbf{U})$.

Based on these two identities, we can efficiently compute the inverse and Jacobian determinant

$$\begin{aligned} \mathbf{x}_c &= \mathbf{y}(\mathbf{I}^{(s)} - \mathbf{U}^{(s)}(\mathbf{I}^{(d_s)} + \mathbf{V}^{(s)}\mathbf{U}^{(s)})^{-1}\mathbf{V}^{(s)}), \\ \mathbf{x} &= (\mathbf{I}^{(c)} - \mathbf{U}^{(c)}(\mathbf{I}^{(d_c)} + \mathbf{V}^{(c)}\mathbf{U}^{(c)})^{-1}\mathbf{V}^{(c)})\mathbf{x}_c, \end{aligned} \quad (6)$$

and

$$\log \left| \det \left(\frac{\partial \mathbf{y}}{\partial \mathbf{x}} \right) \right| = n \log \left| \det(\mathbf{I}^{(d_c)} + \mathbf{V}^{(c)}\mathbf{U}^{(c)}) \right| + c \log \left| \det(\mathbf{I}^{(d_s)} + \mathbf{V}^{(s)}\mathbf{U}^{(s)}) \right|, \quad (7)$$

where $\mathbf{I}^{(d_c)}$ and $\mathbf{I}^{(d_s)}$ are d_c - and d_s -dimensional identity matrices, respectively.

A Woodbury transformation is also a generalized permutation layer. We can directly replace an invertible convolution in Figure 1a with a Woodbury transformation. In contrast with 1×1 convolutions, Woodbury transformations are able to model correlations along both channel and spatial axes. We illustrate this in Figure 2. To implement Woodbury transformations, we need to store four weight matrices, i.e., $\mathbf{U}^{(c)}$, $\mathbf{U}^{(s)}$, $\mathbf{V}^{(c)}$, and $\mathbf{V}^{(s)}$. To simplify our analysis, let $d_c \leq d$ and $d_s \leq d$, where d is a constant. This setting is also consistent with our experiments. The size of $\mathbf{U}^{(c)}$ and $\mathbf{V}^{(c)}$ is $\mathcal{O}(dc)$, and the size of $\mathbf{U}^{(s)}$ and $\mathbf{V}^{(s)}$ is $\mathcal{O}(dn)$. The space complexity is $\mathcal{O}(d(c+n))$.

For training and likelihood computation, the main computational bottleneck is computing \mathbf{y} and the Jacobian determinant. To compute \mathbf{y} with Equation 4, we need to first compute the channel transformation and then compute the spatial transformation. The computational complexity is $\mathcal{O}(dcn)$. To compute the determinant with Equation 7, we need to first compute the matrix product of \mathbf{V} and \mathbf{U} , and then compute the determinant. The computational complexity is $\mathcal{O}(d^2(c+n) + d^3)$.

For sampling, we need to compute the inverse transformations, i.e., Equation 6. With the Woodbury identity, we actually only need to compute the inverses of $\mathbf{I}^{(d_s)} + \mathbf{V}^{(s)}\mathbf{U}^{(s)}$ and $\mathbf{I}^{(d_c)} + \mathbf{V}^{(c)}\mathbf{U}^{(c)}$, which are computed with time complexity $\mathcal{O}(d^3)$. To implement the inverse transformations, we can compute the matrix chain multiplication, so we can avoid computing the product of two large matrices twice, yielding cost $\mathcal{O}(c^2 + n^2)$. For example, for the inverse spatial transformation, we can compute it as $\mathbf{x}_c = \mathbf{y} - ((\mathbf{y}\mathbf{U}^{(s)})(\mathbf{I}^{(d_s)} + \mathbf{V}^{(s)}\mathbf{U}^{(s)})^{-1})\mathbf{V}^{(s)}$, so that its complexity is $\mathcal{O}(d^3 + cd^2 + cnd)$. The total computational complexity of Equation 6 is $\mathcal{O}(dcn + d^2(n+c) + d^3)$.

In practice, we found that for a high-dimensional input, a relatively small d is enough to obtain good performance, e.g., the input is $256 \times 256 \times 3$ images, and $d = 16$. In this situation, $nc \geq d^3$. Therefore, we can omit d and approximately see the spatial complexity as $\mathcal{O}(c+n)$, and the forward or inverse transformation as $\mathcal{O}(nc)$. They are all linear to the input size.

We do not restrict \mathbf{U} and \mathbf{V} to force \mathbf{W} to be invertible. Based on analysis by Hoogeboom et al. [15], the training maximizes the log-likelihood, which implicitly pushes $\det(\mathbf{I} + \mathbf{V}\mathbf{U})$ away from 0. Therefore, it is not necessary to explicitly force invertibility. In our experiments, the Woodbury transformations are as robust as other invertible convolution layers.

¹A more general version replaces $\mathbf{I}^{(n)}$ and $\mathbf{I}^{(k)}$ with arbitrary invertible $n \times n$ and $k \times k$ matrices. But this simplified version is sufficient for our tasks.

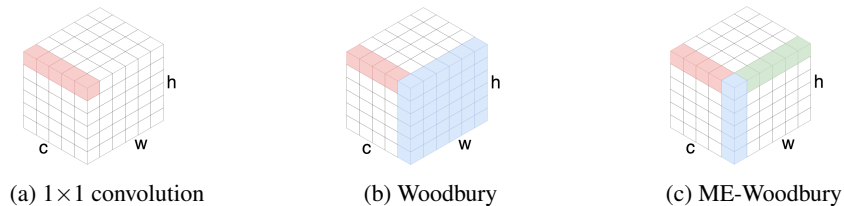


Figure 2: Visualization of three transformations. The 1×1 convolution only operates along the channel axis. The Woodbury transformation operates along both the channel and spatial axes, modeling the dependencies of one channel directly via one transformation. The ME-Woodbury transformation operates along three axes. It uses two transformations to model spatial dependencies.

3.3 Memory-Efficient Variant

In Eq. 4, one potential challenge arises from the sizes of $\mathbf{U}^{(s)}$ and $\mathbf{V}^{((s))}$, which are linear in n . The challenge is that n may be large in some practical problems, e.g., high-resolution images. We develop a memory-efficient variant of Woodbury transformations, i.e., ME-Woodbury, to solve this problem. The ME version can effectively reduce space complexity from $\mathcal{O}(d(c + hw))$ to $\mathcal{O}(d(c + h + w))$.

The difference between ME-Woodbury transformations and Woodbury transformations is that the ME form cannot directly model spatial correlations. As shown in Figure 2c, it uses two transformations, for height and width, together to model the spatial correlations. Therefore, for a specific channel k , when two dimensions $\mathbf{x}_{k,i,j}$ and $\mathbf{x}_{k,u,v}$ are in two different heights, and widths, their interaction will be modeled indirectly. In our experiments, we found that this limitation only slightly impacts ME-Woodbury’s performance. More details on ME-Woodbury transformations are in the appendix.

4 Related Work

Rezende and Mohamed [30] developed planar flows for variational inference $\mathbf{z}_{t+1} = \mathbf{z}_t + \mathbf{u}\delta(\mathbf{w}^T \mathbf{z}_t + b)$, where \mathbf{z} , \mathbf{w} , and \mathbf{u} are d -dimensional vectors, $\delta(\cdot)$ is an activation function, and b is a scalar.

Berg et al. [3] generalized these to Sylvester flows $\mathbf{z}_{t+1} = \mathbf{z}_t + \mathbf{QR}\delta(\tilde{\mathbf{R}}\mathbf{Q}^T \mathbf{z}_t + \mathbf{r})$, where \mathbf{R} and $\tilde{\mathbf{R}}$ are upper triangular matrices, \mathbf{Q} is composed of a set of orthonormal vectors, and \mathbf{r} is a d -dimensional vector. The resulting Jacobian determinant can be efficiently computed via Sylvester’s identity, just as our methods do. However, Woodbury transformations have key differences from Sylvester flows. First, Berg et al. only analyze their models on vectors. The inputs to our layers are matrices, so our method operates on high-dimensional input, e.g., images. Second, though Sylvester flows are inverse functions, computing their inverse is difficult. One possible way is to apply iterative methods [2, 5, 34] to compute the inverse. But this research direction is unexplored. Our layers can be inverted efficiently with the Woodbury identity. Third, our layers do not restrict the transformation matrices to be triangular or orthogonal. In fact, Woodbury transformations can be seen as another generalized variant of planar flows on matrices, with $\delta(\mathbf{x}) = \mathbf{x}$, and whose inverse is tractable. Roughly speaking, Woodbury transformations can also be viewed as applying the planar flows sequentially to each row of the input matrix. After this work was completed and submitted, we learned that the TensorFlow software [1] also uses the Woodbury identity in their affine bijector.

Normalizing flows have also been used for variational inference, density estimation, and generative modeling. Autoregressive flows [17, 23, 25, 29] restrict each variable to depend on those that precede it in a sequence, forcing a triangular Jacobian. Non-linear coupling layers replace the affine transformation function. Specifically, spline flows [8, 26] use spline interpolation, and Flow++ [14] uses a mixture cumulative distribution function to define these functions. Flow++ also uses variational dequantization to prevent model collapse. Many works [9, 15, 18, 22] develop invertible convolutional flows to model interactions among dimensions. MintNet [34] is a flexible architecture composed of multiple masked invertible layers. I-ResNet [2, 5] uses discriminative deep network architecture as the flow. These two models require iterative methods to compute the inverse. Discrete flows [16, 36] and latent flows [41] can be applied to discrete data such as text. Continuous-time flows [4, 12] have been developed based on the theory of ordinary differential equations.

5 Experiments

In this section, we compare the performance of Woodbury transformations against other modern flow architectures, measuring running time, bit per-dimension (\log_2 -likelihood), and sample quality.

Running Time We follow Finz et al. [9] and compare the per-sample running time of Woodbury transformations to other generalized permutations: 1×1 [22], emerging [15], and periodic convolutions [9, 15]. We test the training time and sampling time. In training, we compute (1) forward propagation $f(\cdot)$, (2) the Jacobian determinant, i.e., $\det\left(\frac{\partial \mathbf{y}}{\partial \mathbf{x}}\right)$, and (3) the gradient of parameters. For sampling, we compute the inverse of transformation $\mathbf{x} = f^{-1}(\mathbf{y})$. For emerging and periodic convolutions, we use 3×3 kernels. For Woodbury transformations, we fix the latent dimension $d = 16$. For fair comparison, we implement all methods in Pytorch and run them on an Nvidia Titan V GPU. We follow Hooeboom et al. [15] and implement the emerging convolution inverse in Cython, and we compute it on a 4 Ghz CPU (the GPU version is slower than the Cython version). We first fix the spatial size to be 64×64 and vary the channel number. We then fix the channel number to be 96 and vary the spatial size.

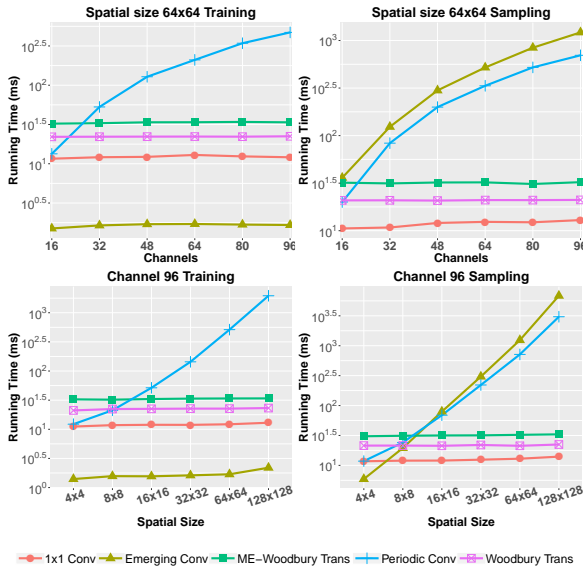


Figure 3: Running time comparison. Sampling with emerging convolutions is slow, since their inverses are not parallelizable. Periodic convolutions are costly for larger inputs. Both 1×1 convolutions and Woodbury transformations are efficient in training and sampling.

The results are shown in Figure 3. For training, the emerging convolution is the fastest. This is because its Jacobian is a triangular matrix, so computing its determinant is much more efficient than other methods. The Woodbury transformation and ME-Woodbury are slightly slower than the 1×1 convolution, since they contain more transformations. Emerging convolutions, Woodbury transformations, and 1×1 convolutions only slightly increase with input size, rather than increasing with $\mathcal{O}(c^3)$. This invariance to input size is likely because of how the GPU parallelizes computation. The periodic convolution is efficient only when the input size is small. When the size is large, it becomes slow, e.g., when the input size is $96 \times 64 \times 64$, it is around 30 times slower than Woodbury transformations. In our experiments, we found that the Fourier transformation requires a large amount of memory. According to Finz et al. [9], the Fourier step may be the bottleneck that impacts periodic convolution’s scalability. A more efficient implementation of Fourier transformation, e.g., [18], may improve its running time.

For sampling, both 1×1 convolutions and Woodbury transformations are efficient. The 1×1 convolution is the fastest, and the Woodbury transformations are only slightly slower. Neither is sensitive to the change of input size. Emerging convolutions and periodic convolutions are much slower than Woodbury transformations, and their running time increases with the input size. When the input size is $96 \times 128 \times 128$, they are around 100 to 200 times slower than Woodbury transformations. This difference is because emerging convolutions cannot make use of parallelization, and periodic transformations require conversion to Fourier form. Based on these results, we can conclude that both emerging convolution and periodic convolution do not scale well to high-dimensional inputs. In contrast, Woodbury transformations are efficient in both training and sampling.

Quantitative Evaluation

We compare Woodbury transformations with state-of-the-art flow models, measuring bit per-dimension (bpd). We train with the CIFAR-10 [24] and ImageNet [32] datasets. We compare with three generalized permutation methods— 1×1 convolution, emerging convolution, and periodic convolution—and two coupling layers—neural spline coupling [8] and MaCow [25]. We use Glow (Fig. 1, [22]) as the basic flow architecture. For each method, we replace the corresponding layer.

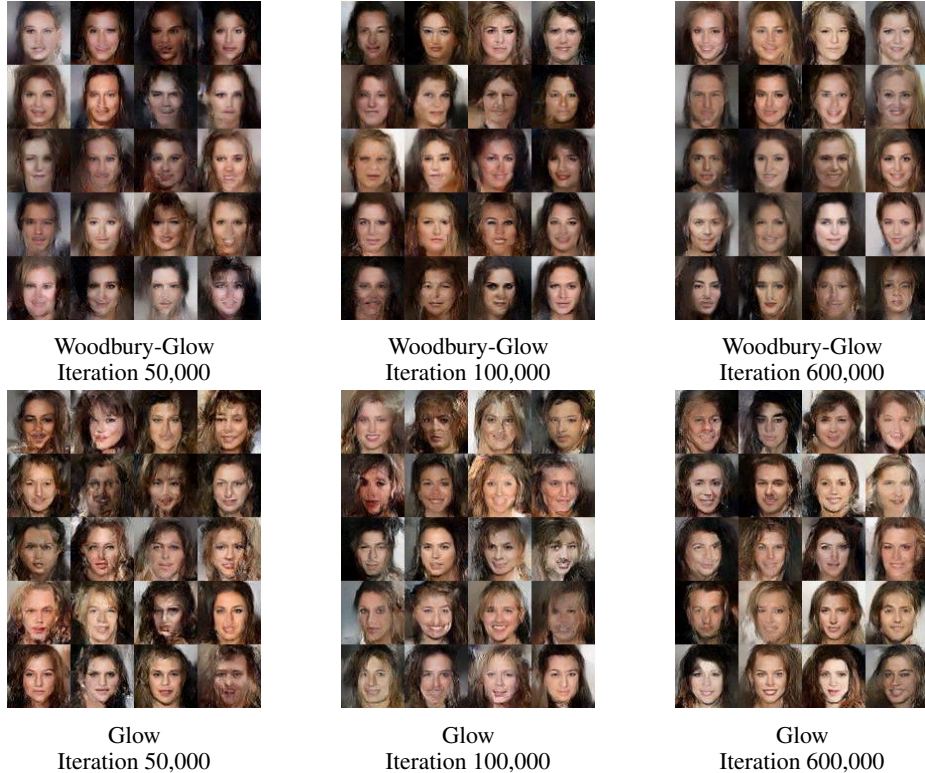


Figure 4: Random samples 64×64 drawn from models trained on CelebA with temperature 0.7.

For example, to construct a flow with Woodbury transformations, we replace the 1×1 convolution with a Woodbury transformation, i.e., Eq. 4. For all generalized permutation methods, we use affine coupling. For each of the coupling layer baselines, we substitute it for the affine coupling. We tune the parameters of neural spline coupling and MaCow so that their sizes are close to affine coupling. We follow Hooeboom et al. [15] and test the performance of small models. For 32×32 images, we set the number of levels to $L = 3$ and the number of steps per-level to $K = 8$. For 64×64 images, we use $L = 4$ and $K = 16$. More details are in the appendix.

Table 1: Quantitative evaluation results.

	Quantitative measure (bpd)			Model sizes (# parameters)	
	CIFAR-10 32x32	ImageNet 32x32	ImageNet 64x64	32x32 images	64x64 images
1×1 convolution	3.51	4.32	3.94	11.02M	37.04M
Emerging	3.48	4.26	3.91	11.43M	40.37M
Periodic	3.49	4.28	3.92	11.21M	38.61M
Neural spline	3.50	4.24	3.95	10.91M	38.31M
MaCow	3.48	4.34	4.15	11.43M	37.83M
ME-Woodbury	3.48	4.22	3.91	11.02M	36.98M
Woodbury	3.47	4.20	3.87	11.10M	37.60M

The test-set likelihoods are listed in Table 1 left. Our scores are worse than those reported by Hooeboom et al. [15], Kingma and Dhariwal [22] because we use smaller models and train each model on a single GPU. Based on the scores, 1×1 convolutions perform the worst. Emerging convolutions and periodic convolutions score better than the 1×1 convolutions, since they are more flexible and can model the dependencies along the spatial axes. Neural spline coupling works well on 32×32 images, but do slightly worse than 1×1 convolution on 64×64 images. MaCow does not work well on ImageNet. This trend demonstrates the importance of permutation layers. They can model the interactions among dimensions and shuffle them, which coupling layers cannot do. Without

a good permutation layer, a better coupling layer still cannot always improve the performance. The Woodbury transformation models perform the best, likely because they can model the interactions between the target dimension and all other dimensions, while the invertible convolutions only model the interactions between target dimension its neighbors. ME-Woodbury performs only slightly worse than the full version, showing that its restrictions provide a useful tradeoff between model quality and efficiency.

We list model sizes in Table 1 (right). Despite modeling rich interactions, Woodbury transformations are not the largest. With 32×32 images, ME-Woodbury and 1×1 convolution are the same size. When the image size is 64×64 , ME-Woodbury is the smallest. This is because we use the multi-scale architecture, i.e., Fig. 1, to combine layers. The squeeze layer doubles the input variable’s channels at each level, so larger L suggests larger c . The space complexities of invertible convolutions are $\mathcal{O}(c^2)$, while the space complexity of ME-Woodbury is linear to c . When c is large, the weight matrices of invertible convolutions are larger than the weight matrices of ME-Woodbury.

Latent Dimension Evaluation We test the impact of latent dimension d on the performance of Woodbury-Glow. We train our models on CIFAR-10, and use bpd as metric. We vary d within $\{2, 4, 8, 16, 32\}$. The results are in Table 2. When $d < 8$, the model performance will be impacted. When $d > 16$, increasing d will not improve the bpd. This is probably because when d is too small, the latent features cannot represent the input variables well, and when d is too big, the models become hard to train. When $8 \leq d \leq 16$, the Woodbury transformations are powerful enough to model the interactions among dimensions. We also test two values of d , i.e., 16, 32, of Woodbury-Glow on ImageNet 64×64 . The bpd of both d are 3.87, which are consistent with our conclusion.

Table 2: Evaluation of different d (bpd).

	Woodbury	ME-Woodbury
$d = 2$	3.54	3.53
$d = 4$	3.51	3.51
$d = 8$	3.48	3.48
$d = 16$	3.47	3.48
$d = 32$	3.47	3.48

Sample Quality Comparisons We train Glow and Woodbury-Glow on the CelebA-HQ dataset [19]. We use 5-bit images and set the size of images to be 64×64 , 128×128 , and 256×256 . Due to our limited computing resources, we use relatively small models in our experiments. We follow Kingma and Dhariwal [22] and choose a temperature parameter to encourage higher quality samples. Detailed parameter settings are in the appendix. We compare samples from Glow and Woodbury-Glow during three phases of training, displayed in Fig. 4. The samples show a clear trend where Woodbury-Glow more quickly learns to generate reasonable face shapes. After 100,000 iterations, it can already generate reasonable samples, while Glow’s samples are heavily distorted. Woodbury-Glow samples are consistently smoother and more realistic than samples from Glow in all phases of training. The samples demonstrate Woodbury transformations’ advantages. The learning curves in Figure 5 also show that the NLL of Woodbury Glow decreases faster, which is consistent to the sample comparisons. In the appendix, we show analogous comparisons using higher resolution versions of CelebA data, which also exhibit the trend of Woodbury-Glow generating more realistic images than Glow at the same training iterations.

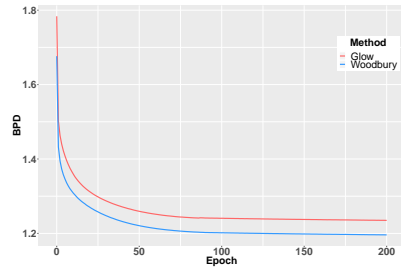


Figure 5: Learning curves on CelebA-HQ 64×64 . The NLL of Woodbury Glow decreases faster than Glow.

6 Conclusion

In this paper, we develop Woodbury transformations, which use the Woodbury matrix identity to compute the inverse transformations and Sylvester’s determinant identity to compute Jacobian determinants. Our method has the same advantages as invertible $d \times d$ convolutions that can capture correlations among all dimensions. In contrast to the invertible $d \times d$ convolutions, our method is parallelizable and the computational complexity of our methods are linear to the input size, so that it is still efficient in computation when the input is high-dimensional. One potential limitation is that Woodbury transformations do not have parameter sharing scheme as in convolutional layers, so one potential future research is to develop partially Woodbury transformations that can share parameters. We test our models on multiple image datasets and they outperform state-of-the-art methods.

Broader Impact

This paper presents fundamental research on increasing the expressiveness of deep probabilistic models. Its impact is therefore linked to the various applications of such models. By enriching the class of complex deep models for which we can train with exact likelihood, we may enable a wide variety of applications that can benefit from modeling of uncertainty. However, a potential danger of this research is that deep generative models have been recently applied to synthesize realistic images and text, which can be used for misinformation campaigns.

Acknowledgments

We thank NVIDIA’s GPU Grant Program and Amazon’s AWS Cloud Credits for Research program for their support. The work was completed while both authors were affiliated with the Virginia Tech Department of Computer Science.

References

- [1] Martín Abadi, Paul Barham, Jianmin Chen, Zhifeng Chen, Andy Davis, Jeffrey Dean, Matthieu Devin, Sanjay Ghemawat, Geoffrey Irving, Michael Isard, et al. Tensorflow: A system for large-scale machine learning. In *12th USENIX Symposium on Operating Systems Design and Implementation*, pages 265–283, 2016.
- [2] Jens Behrmann, Will Grathwohl, Ricky TQ Chen, David Duvenaud, and Jörn-Henrik Jacobsen. Invertible residual networks. *arXiv preprint arXiv:1811.00995*, 2018.
- [3] Rianne van den Berg, Leonard Hasenclever, Jakub M Tomczak, and Max Welling. Sylvester normalizing flows for variational inference. *arXiv preprint arXiv:1803.05649*, 2018.
- [4] Tian Qi Chen, Yulia Rubanova, Jesse Bettencourt, and David K Duvenaud. Neural ordinary differential equations. In *Advances in Neural Information Processing Systems*, pages 6571–6583, 2018.
- [5] Tian Qi Chen, Jens Behrmann, David K Duvenaud, and Jörn-Henrik Jacobsen. Residual flows for invertible generative modeling. In *Advances in Neural Information Processing Systems*, pages 9913–9923, 2019.
- [6] Laurent Dinh, David Krueger, and Yoshua Bengio. NICE: Non-linear independent components estimation. *arXiv preprint arXiv:1410.8516*, 2014.
- [7] Laurent Dinh, Jascha Sohl-Dickstein, and Samy Bengio. Density estimation using real NVP. *arXiv preprint arXiv:1605.08803*, 2016.
- [8] Conor Durkan, Artur Bekasov, Iain Murray, and George Papamakarios. Neural spline flows. *arXiv preprint arXiv:1906.04032*, 2019.
- [9] Marc Finz, Pavel Izmailov, Wesley Maddox, Polina Kirichenko, and Andrew Gordon Wilson. Invertible convolutional networks. In *ICML Workshop on Invertible Neural Networks and Normalizing Flows*, 2019.
- [10] Mathieu Germain, Karol Gregor, Iain Murray, and Hugo Larochelle. Made: Masked autoencoder for distribution estimation. In *International Conference on Machine Learning*, pages 881–889, 2015.
- [11] Ian Goodfellow, Jean Pouget-Abadie, Mehdi Mirza, Bing Xu, David Warde-Farley, Sherjil Ozair, Aaron Courville, and Yoshua Bengio. Generative adversarial nets. In *Advances in Neural Information Processing Systems*, pages 2672–2680, 2014.
- [12] Will Grathwohl, Ricky TQ Chen, Jesse Bettencourt, Ilya Sutskever, and David Duvenaud. Ffjord: Free-form continuous dynamics for scalable reversible generative models. *arXiv preprint arXiv:1810.01367*, 2018.
- [13] Alex Graves. Generating sequences with recurrent neural networks. *arXiv preprint arXiv:1308.0850*, 2013.
- [14] Jonathan Ho, Xi Chen, Aravind Srinivas, Yan Duan, and Pieter Abbeel. Flow++: Improving flow-based generative models with variational dequantization and architecture design. *arXiv preprint arXiv:1902.00275*, 2019.

- [15] Emiel Hoogeboom, Rianne van den Berg, and Max Welling. Emerging convolutions for generative normalizing flows. *arXiv preprint arXiv:1901.11137*, 2019.
- [16] Emiel Hoogeboom, Jorn WT Peters, Rianne van den Berg, and Max Welling. Integer discrete flows and lossless compression. *arXiv preprint arXiv:1905.07376*, 2019.
- [17] Chin-Wei Huang, David Krueger, Alexandre Lacoste, and Aaron Courville. Neural autoregressive flows. *arXiv preprint arXiv:1804.00779*, 2018.
- [18] Mahdi Karami, Dale Schuurmans, Jascha Sohl-Dickstein, Laurent Dinh, and Daniel Duckworth. Invertible convolutional flow. In *Advances in Neural Information Processing Systems*, pages 5636–5646, 2019.
- [19] Tero Karras, Timo Aila, Samuli Laine, and Jaakko Lehtinen. Progressive growing of gans for improved quality, stability, and variation. *arXiv preprint arXiv:1710.10196*, 2017.
- [20] Diederik Kingma and Jimmy Ba. Adam: A method for stochastic optimization. *arXiv preprint arXiv:1412.6980*, 2014.
- [21] Diederik P Kingma and Max Welling. Auto-encoding variational Bayes. *arXiv preprint arXiv:1312.6114*, 2013.
- [22] Durk P Kingma and Prafulla Dhariwal. Glow: Generative flow with invertible 1x1 convolutions. In *Advances in Neural Information Processing Systems*, pages 10215–10224, 2018.
- [23] Durk P Kingma, Tim Salimans, Rafal Jozefowicz, Xi Chen, Ilya Sutskever, and Max Welling. Improved variational inference with inverse autoregressive flow. In *Advances in Neural Information Processing Systems*, pages 4743–4751, 2016.
- [24] Alex Krizhevsky, Geoffrey Hinton, et al. Learning multiple layers of features from tiny images. Technical report, Citeseer, 2009.
- [25] Xuezhe Ma, Xiang Kong, Shanghang Zhang, and Eduard Hovy. Macow: Masked convolutional generative flow. In *Advances in Neural Information Processing Systems*, pages 5891–5900, 2019.
- [26] Thomas Müller, Brian McWilliams, Fabrice Rousselle, Markus Gross, and Jan Novák. Neural importance sampling. *ACM Transactions on Graphics (TOG)*, 38(5):1–19, 2019.
- [27] Aaron van den Oord, Sander Dieleman, Heiga Zen, Karen Simonyan, Oriol Vinyals, Alex Graves, Nal Kalchbrenner, Andrew Senior, and Koray Kavukcuoglu. Wavenet: A generative model for raw audio. *arXiv preprint arXiv:1609.03499*, 2016.
- [28] Aaron van den Oord, Nal Kalchbrenner, and Koray Kavukcuoglu. Pixel recurrent neural networks. *arXiv preprint arXiv:1601.06759*, 2016.
- [29] George Papamakarios, Theo Pavlakou, and Iain Murray. Masked autoregressive flow for density estimation. In *Advances in Neural Information Processing Systems*, pages 2338–2347, 2017.
- [30] Danilo Jimenez Rezende and Shakir Mohamed. Variational inference with normalizing flows. *arXiv preprint arXiv:1505.05770*, 2015.
- [31] Danilo Jimenez Rezende, Shakir Mohamed, and Daan Wierstra. Stochastic backpropagation and approximate inference in deep generative models. *arXiv preprint arXiv:1401.4082*, 2014.
- [32] Olga Russakovsky, Jia Deng, Hao Su, Jonathan Krause, Sanjeev Satheesh, Sean Ma, Zhiheng Huang, Andrej Karpathy, Aditya Khosla, Michael Bernstein, et al. Imagenet large scale visual recognition challenge. *International Journal of Computer Vision*, 115(3):211–252, 2015.
- [33] Kihyuk Sohn, Honglak Lee, and Xinchen Yan. Learning structured output representation using deep conditional generative models. In *Advances in Neural Information Processing Systems*, pages 3483–3491, 2015.
- [34] Yang Song, Chenlin Meng, and Stefano Ermon. Mintnet: Building invertible neural networks with masked convolutions. In *Advances in Neural Information Processing Systems*, pages 11002–11012, 2019.
- [35] James Joseph Sylvester. On the relation between the minor determinants of linearly equivalent quadratic functions. *The London, Edinburgh, and Dublin Philosophical Magazine and Journal of Science*, 1(4):295–305, 1851.
- [36] Dustin Tran, Keyon Vafa, Kumar Krishna Agrawal, Laurent Dinh, and Ben Poole. Discrete flows: Invertible generative models of discrete data. *arXiv preprint arXiv:1905.10347*, 2019.

- [37] Max A Woodbury. Inverting modified matrices. 1950.
- [38] Fisher Yu, Yinda Zhang, Shuran Song, Ari Seff, and Jianxiong Xiao. Lsun: Construction of a large-scale image dataset using deep learning with humans in the loop. *arXiv preprint arXiv:1506.03365*, 2015.
- [39] Lantao Yu, Weinan Zhang, Jun Wang, and Yong Yu. Seqgan: Sequence generative adversarial nets with policy gradient. In *Thirty-First AAAI Conference on Artificial Intelligence*, 2017.
- [40] Jun-Yan Zhu, Taesung Park, Phillip Isola, and Alexei A Efros. Unpaired image-to-image translation using cycle-consistent adversarial networks. In *Proceedings of International Conference on Computer Vision*, pages 2223–2232, 2017.
- [41] Zachary M Ziegler and Alexander M Rush. Latent normalizing flows for discrete sequences. *arXiv preprint arXiv:1901.10548*, 2019.

A More Background

In this section, we introduce more detailed background knowledge.

A.1 Normalizing Flows

Let \mathbf{x} be a high-dimensional continuous variable. We suppose that \mathbf{x} is drawn from $p^*(\mathbf{x})$, which is the true data distribution. Given a collected dataset $\mathcal{D} = \{\mathbf{x}_1, \mathbf{x}_2, \dots, \mathbf{x}_D\}$, we are interested in approximating $p^*(\mathbf{x})$ with a model $p_\theta(\mathbf{x})$. We optimize θ by minimizing the negative log-likelihood

$$\mathcal{L}(\mathcal{D}) = \sum_{i=1}^D -\log p_\theta(\mathbf{x}_i). \quad (8)$$

For some settings, variable $\tilde{\mathbf{x}}$ is discrete, e.g., image pixel values are often integers. In these cases, we dequantize $\tilde{\mathbf{x}}$ by adding continuous noise $\boldsymbol{\mu}$ to it, resulting in a continuous variable $\mathbf{x} = \tilde{\mathbf{x}} + \boldsymbol{\mu}$. As shown by Ho et al. [14], the log-likelihood of $\tilde{\mathbf{x}}$ is lower-bounded by the log-likelihood of \mathbf{x} .

Normalizing flows enable computation of $p_\theta(\mathbf{x})$, even though it is usually intractable for many other model families. A normalizing flow [30] is composed of a series of invertible functions $\mathbf{f} = \mathbf{f}_1 \circ \mathbf{f}_2 \circ \dots \circ \mathbf{f}_K$, which transform \mathbf{x} to a latent code \mathbf{z} drawn from a simple distribution. Therefore, with the *change of variables* formula, we can rewrite $\log p_\theta(\mathbf{x})$ to be

$$\log p_\theta(\mathbf{x}) = \log p_Z(\mathbf{z}) + \sum_{i=1}^K \log \left| \det \left(\frac{\partial \mathbf{f}_i}{\partial \mathbf{r}_{i-1}} \right) \right|, \quad (9)$$

where $\mathbf{r}_i = \mathbf{f}_i(\mathbf{r}_{i-1})$, $\mathbf{r}_0 = \mathbf{x}$, and $\mathbf{r}_K = \mathbf{z}$.

A.2 Invertible $d \times d$ Convolutions

Emerging convolutions [15] combine two autoregressive convolutions [10, 23]. Formally,

$$\mathbf{M}'_1 = \mathbf{M}_1 \odot \mathbf{A}_1, \quad \mathbf{M}'_2 = \mathbf{M}_2 \odot \mathbf{A}_2, \quad \mathbf{y} = \mathbf{M}'_2 \star (\mathbf{M}'_1 \star \mathbf{x}),$$

where $\mathbf{M}_1, \mathbf{M}_2$ are convolutional kernels whose size is $c \times c \times d \times d$, and $\mathbf{A}_1, \mathbf{A}_2$ are binary masks. The symbol \star represents the convolution operator.² An emerging convolutional layer has the same receptive fields as standard convolutional layers, which can capture correlations between a target pixel and its neighbor pixels. However, like other autoregressive convolutions, computing the inverse of an emerging convolution requires sequentially traversing each dimension of input, so its computation is not parallelizable and is a computational bottleneck when the input is high-dimensional.

Periodic convolutions [9, 15] use discrete Fourier transformations to transform both the input and the kernel to Fourier domain. A periodic convolution is computed as

$$\mathbf{y}_{u, :, :} = \sum_v \mathcal{F}^{-1}(\mathcal{F}(\mathbf{M}_{u, v, :, :}^{(p)}) \odot \mathcal{F}(\mathbf{x}_{v, :, :})),$$

where \mathcal{F} is a discrete Fourier transformation, and $\mathbf{M}^{(p)}$ is the convolution kernel whose size is $c \times c \times d \times d$. The computational complexity of periodic convolutions is $\mathcal{O}(c^2 h w \log(h w) + c^3 h w)$. In our experiments, we found that the Fourier transformation requires a large amount of memory. These two problems impact the efficiency of both training and sampling when the input is high-dimensional.

B Memory-Efficient Woodbury Transformations

Memory-Efficient Woodbury transformations can effectively reduce the space complexity. The main idea is to perform spatial transformations along the height and width axes separately, i.e., a height

²In practice, a convolutional layer is usually implemented as an aggregation of cross-correlations. We follow Hoogeboom et al. [15] and omit this detail.

transformation and a width transformation. The transformations are:

$$\begin{aligned}
\mathbf{x}_c &= (\mathbf{I}^{(c)} + \mathbf{U}^{(c)}\mathbf{V}^{(c)})\mathbf{x}, \\
\mathbf{x}_w &= \text{reshape}(\mathbf{x}_c, (ch, w)), \\
\mathbf{x}_w &= \mathbf{x}_c(\mathbf{I}^{(w)} + \mathbf{U}^{(w)}\mathbf{V}^{(w)}), \\
\mathbf{x}_h &= \text{reshape}(\mathbf{x}_w, (cw, h)), \\
\mathbf{y} &= \mathbf{x}_h(\mathbf{I}^{(h)} + \mathbf{U}^{(h)}\mathbf{V}^{(h)}), \\
\mathbf{y} &= \text{reshape}(\mathbf{y}, (c, hw)),
\end{aligned} \tag{10}$$

where $\text{reshape}(\mathbf{x}, (n, m))$ reshapes \mathbf{x} to be an $n \times m$ matrix. Matrices $\mathbf{I}^{(w)}$ and $\mathbf{I}^{(h)}$ are w - and h -dimensional identity matrices, respectively. Matrices $\mathbf{U}^{(w)}$, $\mathbf{V}^{(w)}$, $\mathbf{U}^{(h)}$, and $\mathbf{V}^{(h)}$ are $w \times d_w$, $d_w \times w$, $w \times d_w$, and $d_w \times w$ matrices, respectively, where d_w and d_h are constant latent dimensions.

Using the Woodbury matrix identity and the Sylvester’s determinant identity, we can compute the inverse and Jacobian determinant:

$$\begin{aligned}
\mathbf{y} &= \text{reshape}(\mathbf{y}, (cw, h)), \\
\mathbf{x}_h &= \mathbf{y}(\mathbf{I}^{(h)} - \mathbf{U}^{(h)}(\mathbf{I}^{(d_h)} + \mathbf{V}^{(h)}\mathbf{U}^{(h)})^{-1}\mathbf{V}^{(h)}), \\
\mathbf{x}_w &= \text{reshape}(\mathbf{x}_h, (ch, w)), \\
\mathbf{x}_w &= \mathbf{x}_w(\mathbf{I}^{(w)} - \mathbf{U}^{(w)}(\mathbf{I}^{(d_w)} + \mathbf{V}^{(w)}\mathbf{U}^{(w)})^{-1}\mathbf{V}^{(w)}), \\
\mathbf{x}_c &= \text{reshape}(\mathbf{x}_w, (c, hw)), \\
\mathbf{x} &= (\mathbf{I}^{(c)} - \mathbf{U}^{(c)}(\mathbf{I}^{(d_c)} + \mathbf{V}^{(c)}\mathbf{U}^{(c)})^{-1}\mathbf{V}^{(c)})\mathbf{x}_c,
\end{aligned} \tag{11}$$

$$\begin{aligned}
\log \left| \det \left(\frac{\partial \mathbf{y}}{\partial \mathbf{x}} \right) \right| &= hw \log |\det(\mathbf{I}^{(d_c)} + \mathbf{V}^{(c)}\mathbf{U}^{(c)})| + ch \log |\det(\mathbf{I}^{(d_w)} + \mathbf{V}^{(w)}\mathbf{U}^{(w)})| \\
&\quad + cw \log |\det(\mathbf{I}^{(d_h)} + \mathbf{V}^{(h)}\mathbf{U}^{(h)})|,
\end{aligned} \tag{12}$$

where $\mathbf{I}^{(d_w)}$ and $\mathbf{I}^{(d_h)}$ are d_w - and d_h -dimensional identity matrices, respectively. The Jacobian of the $\text{reshape}()$ is an identity matrix, so its log-determinant is 0.

We call Equation 10 the memory-efficient Woodbury transformation because it reduces space complexity from $\mathcal{O}(c+hw)$ to $\mathcal{O}(c+h+w)$. This method is effective when h and w are large. To analyze its complexity, we let all latent dimensions be less than d as before. The complexity of forward transformation is $\mathcal{O}(dchw)$; the complexity of computing the determinant is $\mathcal{O}(d(c+h+w) + d^3)$; and the complexity of computing the inverse is $\mathcal{O}(dchw + d^2(c+ch+cw) + d^3)$. The same as Woodbury transformations, when the input is high dimensional, we can omit d . Therefore, the computational complexities of the memory-efficient Woodbury transformation are also linear with the input size.

We list the complexities of different methods in Table 3. We can see that the computational complexities of Woodbury transformations are comparable to other methods, and maybe smaller when the input is high-dimensional, i.e., the c, h, w are big.

Table 3: Comparisons of computational complexities.

Method	Forward	Backward
1x1 convolution	$\mathcal{O}(c^2hw + c^3)$	$\mathcal{O}(c^2hw)$
Emerging convolution	$\mathcal{O}(chw \log(hw) + c^3hw)$	$\mathcal{O}(chw \log(hw) + c^2hw)$
Periodic convolution	$\mathcal{O}(c^2hw)$	$\mathcal{O}(c^2hw)$
ME-Woodbury transformation	$\mathcal{O}(dchw)$	$\mathcal{O}(dchw)$
Woodbury transformation	$\mathcal{O}(dchw)$	$\mathcal{O}(dchw)$

C Parameter Settings

In this section, we present additional details about our experiments to aid reproducibility.

C.1 Experiments of Quantitative Evaluation

In the experiments of qualitative evaluation, we compare Woodbury transformations with 3 permutation layer baselines, i.e., 1x1 convolution, emerging convolution, and periodic coupling, and 2 coupling layer baselines, i.e., neural spline coupling, and MaCow. For all generalized permutation methods, we use affine coupling, which is composed of 3 convolutional layers, and the 2 latent layers have 512 channels. For the neural spline coupling, we set the number of spline bins to 4. The spline parameters are generated by a neural network, which is also composed of convolutional layers. For 32×32 images, we set the number of channels to 256, and for 64×64 images, we set it to 224. Ma et al. [25] used steps containing a MaCow unit, i.e., 4 autoregressive convolution coupling layers, and a full Glow step. For fair comparison, we directly use the MaCow unit to replace the affine coupling. For 32×32 images, we set the convolution channel to 384, and for 64×64 images, we set it to 296.

We run each method to fixed number of iterations and test it every 10,000 iterations. The bpd reported in our main paper are the best bpd obtained by each method. The bpd are single-run results. This is because each run of the experiment requires 3 to 5 days, and running each model multiple times is a major cost. We found in our experiments that for the same model and parameter settings, the bpd’s standard deviation of multiple runs are very small, i.e., around 0.003, so single run results are sufficient for comparing bpd.

C.2 Hyper-parameter Settings

We use Adam [20] to tune the learning rates, with $\alpha = 0.001$, $\beta_1 = 0.9$, and $\beta_2 = 0.999$. We use uniform dequantization. The sizes of models we use, and mini-batch sizes for training in our experiments are listed in Table 4.

Table 4: Model sizes and mini-batch sizes.

Dataset	Mini-batch size	Levels(L)	Steps(K)	Coupling channels
CIFAR-10 32x32	64	3	8	512
ImageNet 32x32	64	3	8	512
ImageNet 64x64	32	4	16	512
LSUN Church 96x96	16	5	16	256
CelebA-HQ 64x64	8	4	16	512
CelebA-HQ 128x128	4	5	24	256
CelebA-HQ 256x256	4	6	16	256

C.3 Latent Dimension Settings

In all our experiments, we set the latent dimensions of Woodbury transformations, and ME-Woodbury transformations as in Table 5.

Table 5: Latent dimensions of Woodbury transformations and ME-Woodbury transformations. The numbers in the brackets represent the latent dimension used in that level. For example, the $d_c : \{8, 8, 16\}$, represents that the settings of d_c at the three levels are 8, 8, and 16.

Dataset	Woodbury	ME-Woodbury
CIFAR-10 32x32	$d_c : \{8, 8, 16\}$ $d_s : \{16, 16, 8\}$	$d_c : \{8, 8, 16\}$ $d_h : \{16, 16, 8\}$ $d_w : \{16, 16, 8\}$
ImageNet 32x32	$d_c : \{8, 8, 16\}$ $d_s : \{16, 16, 8\}$	$d_c : \{8, 8, 16\}$ $d_h : \{16, 16, 8\}$ $d_w : \{16, 16, 8\}$
ImageNet 64x64	$d_c : \{8, 8, 16, 16\}$ $d_s : \{16, 16, 8, 8\}$	$d_c : \{8, 8, 16, 16\}$ $d_h : \{16, 16, 8, 8\}$ $d_w : \{16, 16, 8, 8\}$
LSUN Church 96x96	$d_c : \{8, 8, 16, 16, 16\}$ $d_s : \{16, 16, 16, 8, 8\}$	—
CelebA-HQ 64x64	$d_c : \{8, 8, 16, 16\}$ $d_s : \{16, 16, 8, 8\}$	—
CelebA-HQ 128x128	$d_c : \{8, 8, 16, 16, 16\}$ $d_s : \{16, 16, 16, 8, 8\}$	—
CelebA-HQ 256x256	$d_c : \{8, 8, 16, 16, 16, 16\}$ $d_s : \{16, 16, 16, 16, 8, 8\}$	—

D Sample Quality Comparisons

We compare the samples generated by Woodbury-Glow and Glow models trained on the CelebA-HQ dataset. We follow Kingma and Dhariwal [22] and randomly hold out 3,000 images as a test set. We use 5-bit images. We use 64×64 , 128×128 , 256×256 images. Due to our limited computing resources, we use relatively small models. The model sizes and other settings are listed in Table 4 and Table 5. We generate samples from the models during different phases of training and display them in Figure 6, and Figure 7 (The results of 64×64 images are shown in the main paper). For the 128×128 images, both Glow and Woodbury-Glow generate distorted images at iteration 100,000, but Woodbury-Glow seems to improve in later stages, stabilizing the shapes of faces and structure of facial features. Glow, continues generating faces with distorted overall shapes as training continues. For the 256×256 images, neither model ever trains sufficiently to generate highly realistic faces, but Woodbury-Glow makes significantly more progress in these 300,000 iterations than Glow. Glow’s samples at 300,000 are still mostly random swirls with an occasional recognizable face, while almost all of Woodbury-Glow’s samples look like faces, though distorted. Due to limits on our computational resources, we stopped the higher resolution experiments at 300,000 iterations (rather than running to 600,000 iterations as we did for the 64×64 experiments in the main paper). With a larger model and longer training time, it seems Woodbury-Glow would reach higher sample quality much faster than Glow.

The likelihoods of test set under the trained model are listed in Table 3. For the 64×64 and 128×128 images, Woodbury-Glow scores higher likelihood than Glow. For the 256×256 images, their likelihoods are almost identical, and are better than the score reported in [22]. This may be due to three possible reasons: (1) We use affine coupling rather than additive coupling, which is a non-volume preserving layer and may improve the likelihoods; (2) Since the test set is randomly collected, it is different from the one used in [22]; And (3) The model used in [22] is very large, so it may be somewhat over-fitting. Surprisingly, the clear difference in sample quality is not reflected by the likelihoods. This discrepancy may be because we use 5-bit images, and the images are all faces, so the dataset is less complicated than other datasets such as ImageNet. Moreover, even though Glow cannot generate reasonable 256×256 samples, the colors of these samples already match the colors of real images well, so these strange samples may non-intuitively be equivalently likely as the face-like samples from Woodbury-Glow.

Table 6: Bit per-dimension results on CelebA-HQ

Size of images	Glow	Woodbury-Glow
64×64	1.27	1.23
128×128	1.09	1.04
256×256	0.93	0.93

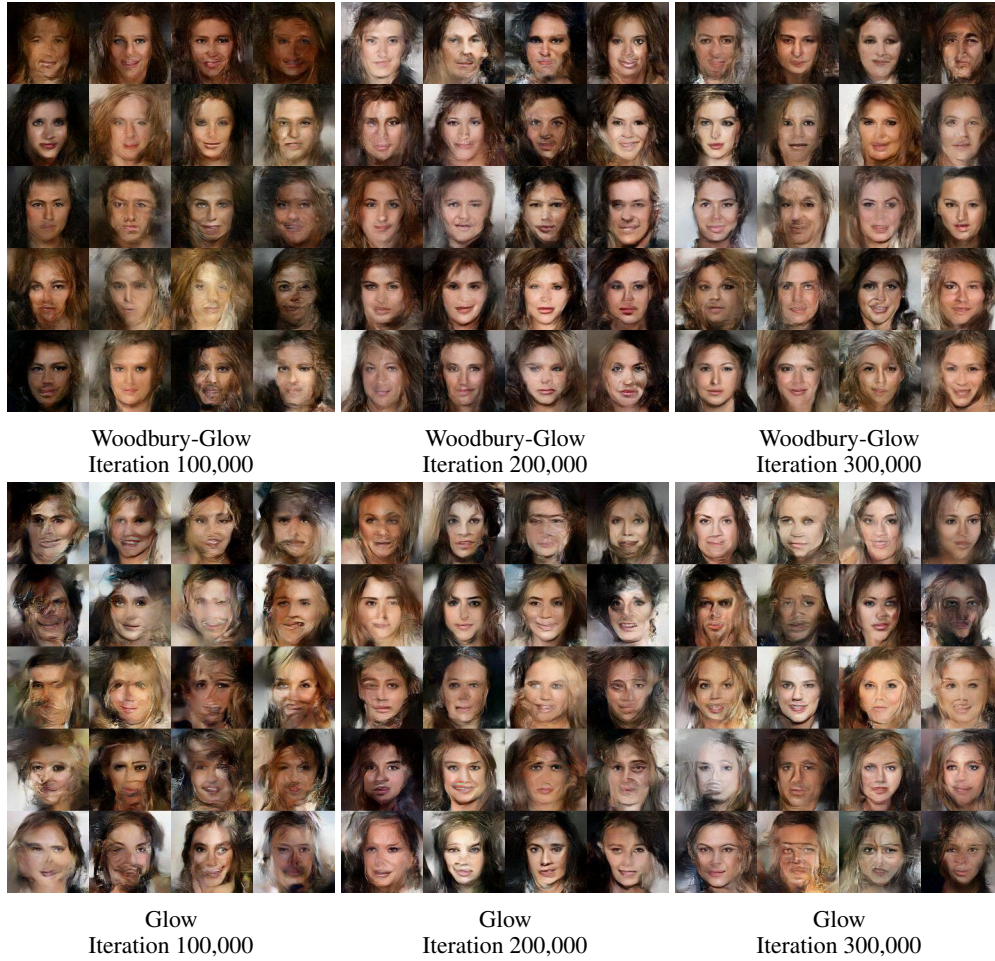


Figure 6: Random samples of 128×128 images drawn with temperature 0.7 from a model trained on CelebA data.



Figure 7: Random samples of 256×256 images drawn with temperature 0.7 from a model trained on CelebA data.

E Additional Samples

In this section, we include additional samples from Woodbury-Glow models trained on our various datasets. These samples complement our quantitative analysis. We train our models on CIFAR-10 [24], ImageNet [32], the LSUN church dataset [38], and the CelebA-HQ dataset [19]. Specifically, for ImageNet, we use 32×32 and 64×64 images. For the LSUN dataset, we use the same approach as Kingma and Dhariwal [22] to resize the images to be 96×96 . For the CelebA-HQ dataset, we use 64×64 , 128×128 , and 256×256 images. For LSUN and CelebA-HQ datasets, we use 5-bit images. The parameter settings of our models are in Table 4 and Table 5. The samples are in Figures 8, 9, 10, 11, 12, 13, and 14.



Figure 8: CIFAR-10 32×32 Woodbury-Glow samples.



Figure 9: ImageNet 32×32 Woodbury-Glow samples.



Figure 10: ImageNet 64×64 Woodbury-Glow samples.



Figure 11: LSUN church 96×96 Woodbury-Glow samples (temperature 0.875).



Figure 12: CelebA-HQ 64×64 Woodbury-Glow samples (temperature 0.7).



Figure 13: CelebA-HQ 128×128 Woodbury-Glow samples (temperature 0.5).



Figure 14: Selected CelebA-HQ 256×256 Woodbury-Glow samples (temperature 0.5).